A three-dimensional model for inductively coupled plasma etching reactors: Azimuthal symmetry, coil properties, and comparison to experiments

Mark J. Kushner,[a] Wenli Z. Collison,[b] and Michael J. Grapperhaus
University of Illinois, Department of Electrical and Computer Engineering, 1406 West Green Street, Urbana, Illinois 61801

John P. Holland and Michael S. Barnes
Lam Research, Inc., 4650 Cushing Parkway, Fremont, California 94538

(Received 4 March 1996; accepted for publication 2 May 1996)

Inductively coupled plasma (ICP) etching reactors are rapidly becoming the tool of choice for low gas pressure, high plasma density etching of semiconductor materials. Due to their symmetry of excitation, these devices tend to have quite uniform etch rates across the wafer. However, side to side and azimuthal variations in these rates have been observed, and have been attributed to various asymmetries in pumping, reactor structure and coil properties. In this article, a three-dimensional computer model for an ICP etching reactor is reported whose purposes is to investigate these asymmetries. The model system is an ICP reactor powered at 13.56 MHz having flat coils of nested annuli powering Ar/N_2 and Cl_2 plasmas over a 20-cm diam wafer. For demonstration purposes, asymmetries were built into the reactor geometry which include a wafer-load lock bay, wafer clamps, electrical feeds to the coil, and specifics of the coil design. Comparisons are made between computed and experimentally measured ion densities and poly-silicon etch rates in Cl_2 plasmas. We find that the electrical transmission line properties of the coil have a large influence on the uniformity of plasma generation and ion fluxes to the wafer. © *1996 American Institute of Physics.*
[S0021-8979(96)08915-3]

I. INTRODUCTION

Inductively coupled plasma (ICP) reactors are being developed as high plasma density (10^{10}–10^{12} cm^{-3}), low gas pressure (< 10's mTorr) sources for etching, and deposition of semiconductor materials.[1–5] ICP plasma etching tools for 20 cm wafers have been demonstrated which have a high degree of uniformity for etch rates and selectivity as a function of azimuth and radius. Azimuthal asymmetries and side-to-side variations in these quantities, however, are not uncommon occurrences during tool development.[6] These asymmetries have been correlated with azimuthal variations in input and pumping of gases, circuit issues related to transmission line matching to the coil, and particulars of the reactor configuration. Modeling of plasma etching reactors, and ICP etch tools in particular, have significantly advanced over the past few years, and many two-dimensional models have been developed.[7–10] These models have been useful in investigating issues related power deposition, transport, and plasma chemistry. However, due to their limited dimensionality these models may not be able to address issues related to reactor asymmetries.

In this article, we describe a three-dimensional, time dependent model for ICP and reactive ion etching (RIE) reactors whose intent is to provide an infrastructure to investigate asymmetries in plasma etching and deposition tools. We discuss here results from the model for ICP reactors which demonstrate the effects of internal structures in the reactor and asymmetries in the inductively coupled electric field on the uniformity of plasma generation and ion densities. Computed ion densities and ion fluxes to the wafer are also compared to Langmuir probe measurements and poly-silicon etch profiles in Cl_2 plasmas. We find that asymmetries in the coil can produce radial or axial electric field components commensurate in magnitude to what is normally assumed to be a symmetric azimuthal component. The transmission line characteristics of the coil can also produce azimuthal variations in the coil current. These conditions produce commensurate variations in the inductively coupled electric field, electron heating, and ion production rates which may persist through the plasma to the plane of the wafer. Coil generated asymmetries in these quantities are reflected in the etch uniformity across the wafer. Geometrical asymmetries, such as wafer clamps and load lock bays for wafer handlers, also cause perturbations in the ion flux. We will describe the model in Sec. II and discuss results from the model for plasma properties in reactors having asymmetries in Sec. III. Comparisons are also made to electric probe measurements of ion densities and etching uniformity. Our concluding remarks are in Sec. IV.

II. DESCRIPTION OF THE MODEL

The model is a three-dimensional extension of a previously described two-dimensional simulation called the Hybrid Plasma Equipment Model (HPEM).[7,11] As a point of departure, the HPEM will first be briefly described followed by modifications we made to that model for the three-dimensional version, called HPEM-3D. The HPEM consists of an electromagnetic module (EMM), an electron Monte

[a]Electronic mail: mjk@uiuc.edu
[b]Present address: Lam Research, Inc., 4650 Cushing Parkway, Freemont, CA 94538.

Carlo simulation (EMCS), and a fluid-chemical kinetics simulation (FKS). The inductively coupled electromagnetic fields are produced by the EMM. Those fields are used in the EMCS to generate the electron energy distribution as a function of position and phase in the radio frequency (rf) cycle. The electron distributions are then used to produce electron transport coefficients and electron impact source functions. These values are transferred to the FKS in which the densities for all charged and neutral species are obtained, and Poisson's equation is solved for the electrostatic fields. The momentum equations for ions and neutral species can also be solved as an option, thereby accounting for inertial effects and gas flow. The densities, conductivities, and electrostatic fields obtained from the FKS are then transferred to the EMM and EMCS. This iterative cycle is repeated until a converged solution is obtained. Another option to the HPEM replaces the EMCS with a Boltzmann–Electron energy equation module (BEM). This option was used for the HPEM-3D, and so will be described below.

The HPEM-3D is functionally equivalent to the HPEM with added dimensionality. The coordinate system may be cylindrical (r,Θ,z) or Cartesian (x,y,z), and in this article results for a cylindrical coordinate system are presented. The EMM of HPEM-3D solves for (r,Θ,z) components of the complex inductively coupled electric field, $\mathbf{E}$. Following the usual procedure,[7–12] a wave equation is formulated from Maxwell's equations by assuming that the charge density $\rho=0$ and that the plasma is collisional. The latter assumption results in currents in the plasma being described by $\mathbf{J}=\sigma\mathbf{E}$, where σ is the conductivity. The wave equation we implemented is

$$\nabla\cdot\frac{1}{\mu}\nabla\mathbf{E}=\frac{\partial^2(\epsilon\mathbf{E})}{\partial t^2}+\frac{\partial(\sigma\mathbf{E}+\mathbf{J}_0)}{\partial t}. \tag{1}$$

J_0 represents externally driven coil currents we obtain from a transmission line model for the coil (see below). Equation (1) is solved in the frequency domain by assuming the electric field is harmonic,

$$\mathbf{E}(\mathbf{r},t)=\mathbf{E}(\mathbf{r})\exp\{i[\omega t+\phi(\mathbf{r})]\}. \tag{2}$$

The conductivity we used is complex and is the sum of the conductivities of each plasma species,

$$\sigma=\sum_j \frac{q^2 n_j}{m_j \nu_j\left(1+\frac{i\omega}{\upsilon_j}\right)}, \tag{3}$$

where n_j, m_j, and ν_j are the density, mass, and momentum transfer collision frequency of species j. This procedure results in three-dimensional partial differential equations for the electric field components $E_{\mathbf{r}}$, E_Z, and E_θ which are iteratively solved in the frequency domain using the method of successive-over-relaxation (SOR).[7]

The externally driven currents in the coil are obtained by representing the coil as a transmission line beginning at the rf generator and terminating at ground.[12] The electrical length of the transmission is mapped to the spatial dimension along the path of the coil. The coil-plasma system is further represented as a single turn transformer.[13] Following conventional transformer theory, the impedance of the secondary (the plasma) can be represented by an equivalent transformed impedance on the primary side of the circuit (the coil). Each discrete element (labeled i) of the transmission line is composed of a sum of impedances

$$Z_i=-i\omega L_{ci}+i/\omega C_{pi}+R_c+Z_{Ti}, \tag{4}$$

where L_c is the physical inductance of the coil, C_p represents capacitive coupling of the coil to the plasma, R_c is Ohmic resistance of the coil, and Z_T is the transformed impedance of the plasma. Apportionment of these quantities along the coil to each element in the transmission line is performed on a geometrical basis. The coil voltage and current (amplitude and phase) of each element along the coil are obtained by solving the resulting circuit equation in the frequency domain. This treatment therefore addresses only the fundamental frequency of excitation. The amplitude of the driving voltage is derived by requiring that the power deposition in the plasma be a specified value. The transmission line currents are then used as driving terms in the solution of the wave equation. These currents are periodically updated during the iterative SOR solution of the wave equation for the electric fields.

The form of the transformed impedance we used has been discussed by Piejak *et al.*[13] The transformed impedance of the plasma is given by

$$Z_T=\left(\frac{\omega M}{Z_p}\right)^2\left[-i\omega L_p+R_p\left(1-i\frac{\omega}{\upsilon_m}\right)\right],\quad M^2=kL_cL_p, \tag{5a}$$

$$Z_p^2=\left(\omega L_p+\frac{\omega}{\upsilon_m}R_p\right)^2+R_p^2, \tag{5b}$$

where L_p is the discharge inductance of the plasma, v_m is the momentum transfer collision frequency in the plasma, R_p is the plasma resistance, and k is the transformer coupling coefficient, estimated to be 0.25 here. We calculated an effective plasma resistance from

$$R_p=\frac{\int \mathbf{j}\cdot\mathbf{E}d^3r}{\frac{1}{2\pi}\int\left(\int \mathbf{j}(\theta)\cdot d\mathbf{A}\right)^2 d\theta}, \tag{6}$$

where $j=\sigma E$ is the plasma current and the integral in the denominator is over the cross sectional area. The numerator is the total power deposition. The denominator is the circulating current. The effect of this integral is to more heavily weight plasma transport coefficients in regions of the plasma where the electric field is large.

In the cases discussed here, the EMCS typically used in the two-dimensional HPEM was replaced by the Boltzmann-electron energy equation module. This decision was made based on the large memory requirements for storing the electron energy distribution at each spatial location in the 3D mesh, and the large number of pseudoparticles required to obtain acceptable statistics. In the BEM, we solve an electron energy equation for average energy ϵ,

$$\frac{\partial(n_e\epsilon)}{\partial t}=P(\epsilon)-n_e\sum_i N_i\kappa_i-\nabla\left(\frac{5}{3}\epsilon\varphi-\lambda\nabla T_e\right), \tag{7}$$

where T_e is the electron temperature [defined as $(2/3)\epsilon$], n_e is the electron density (obtained from the FKS), P is the electron power deposition (obtained from the EMM and FKS), κ_i is the rate coefficient for power loss (eV-cm^{3}s^{-1}) for collisions of electrons with species i having density N_i (the latter obtained from the FKS, λ is the electron thermal conductivity, and φ is the electron flux (obtained from the FKS). This equation is solved in the steady state in three-dimensions using an implicit SOR technique. An electron temperature of 0.05 eV is assigned to all surfaces in contact with the plasma and the thermal conductivity is assigned appropriate values across the sheath commensurate with the electron density in the sheath. This effectively results in an adiabatic boundary condition.

The electron transport coefficients and rate coefficients for use in solving Eq. (7) are obtained by solving Boltzmann's equation (BE) using a two-term spherical harmonic expansion.[14] BE is parameterized over a range of E/N, and a table of transport coefficients as a function of ϵ is constructed. This table is then interpolated during solution of Eq. (7). The electron energy equation and BE (to generate the lookup table) are solved on each iteration through the simulation based on updated densities, mole fractions, fluxes, and power deposition.

Charged and neutral particle densities are generated, and Poisson's equation is solved, in the FKS. To minimize computing resources, the ion momentum equations were not solved in the cases presented here, and so drift-diffusion expressions were used for all species. Poisson's equation is solved using a semi-implicit technique as described in Ref. 7. In doing so, the time step is typically 10^3–10^4 times longer than the dielectric relaxation time. All fluxes and spatial derivatives are couched in finite difference form using a conservative donor cell technique. The transport equations are integrated in time to a quasisteady state solution using acceleration techniques to speed the convergence of the model. Although, the capability exists to rf bias any surface in the reactor, the results presented here will not consider substrate bias; only the coil is powered. Except for the added dimensionality, the algorithms used in the FKS are essentially the same as in the 2D HPEM.

III. ASYMMETRIES IN INDUCTIVELY COUPLED PLASMA REACTORS

The first cases discussed here will be for an idealized ICP reactor, schematically shown in Fig. 1, powered by a flat coil at 13.56 MHz set on top of a quartz window. The wafer is 20 cm in diameter. The substrate to window spacing is 7.5 cm. The gas mixture is Ar/N_2=95/5 at 15 mTorr with a power deposition of 400 W. Although, this is not an etching gas mixture, it does capture many of the features of typical molecular gas mixtures used for etching with the exception of negative ions. The coil has two azimuthal turns, coupled by a radial segment, and is fed by 2 axial current segments. The physical inductance of the coil is $\approx$1.8 μH. Asymmetries have purposely been built into the reactor for demonstration purposes. The first asymmetry is a wafer handler port leading to a load lock. The load lock bay is an opening in the outer wall of the reactor having an extended sized to

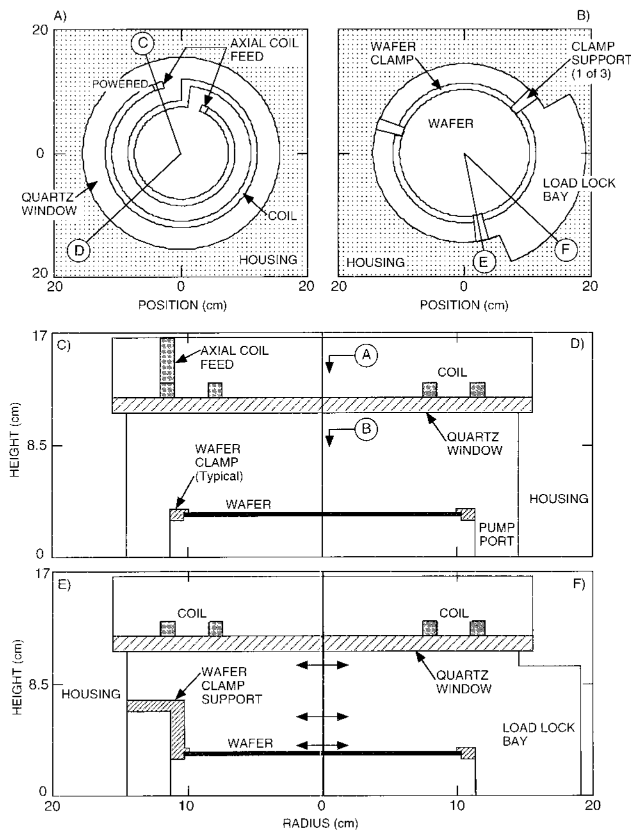

FIG. 1. Schematic of the ICP geometry used in this study. (a) Downward looking view of the top of the coil. The coil has two turns with a radial coupling segment, and is fed by two axial segments. The coil feed along section C is powered; the other feed is terminated. [See (d) for the axial location of this view.] (b) Downward looking view of the chamber from the just below the quartz window. The outline of the wafer clamp support structure, substrate, wafer, and load lock bay are shown. [See (d) for the axial location of this view.] (c)-(f) Radial sections of the reactor at 4 azimuthal locations. [The azimuthal location of the radial sections are shown by the section markers in (a)].

accept the wafer. The second asymmetry consists of 3 dielectric support structures for the wafer clamp. The computational mesh is approximately 45$\times$60 mesh points in the (r,z) plane and 48 θ planes in the azimuthal direction. The species included in the simulation are electrons, Ar, Ar(4s), Ar^+, N_2, and N_2^+. The electron impact and heavy particle reactions for these chemistries are discussed in Refs. 7 and 15. In addition to those processes, we include charge exchange between Ar^+ and N_2, and quenching of Ar(4s) by collisions with N_2.

One of the most important characteristics which determine the azimuthal symmetry of the plasma are the circuit parameters of the coil. Two critical components in this regard are the amount of capacitive coupling from the coil to the plasma (or other metal structures) and the discrete termination impedance to the coil, in these cases a capacitance. Finite capacitive coupling from the coil reduces the conduction current along the path of the coil, thereby reducing the magnitude of the local inductive electric field. This capacitive coupling is controlled, in part by the cross sectional shape of the coil and its proximity to the plasma. The termination capacitance determines the location of the voltage zero crossings (and current maxima) in the standing wave

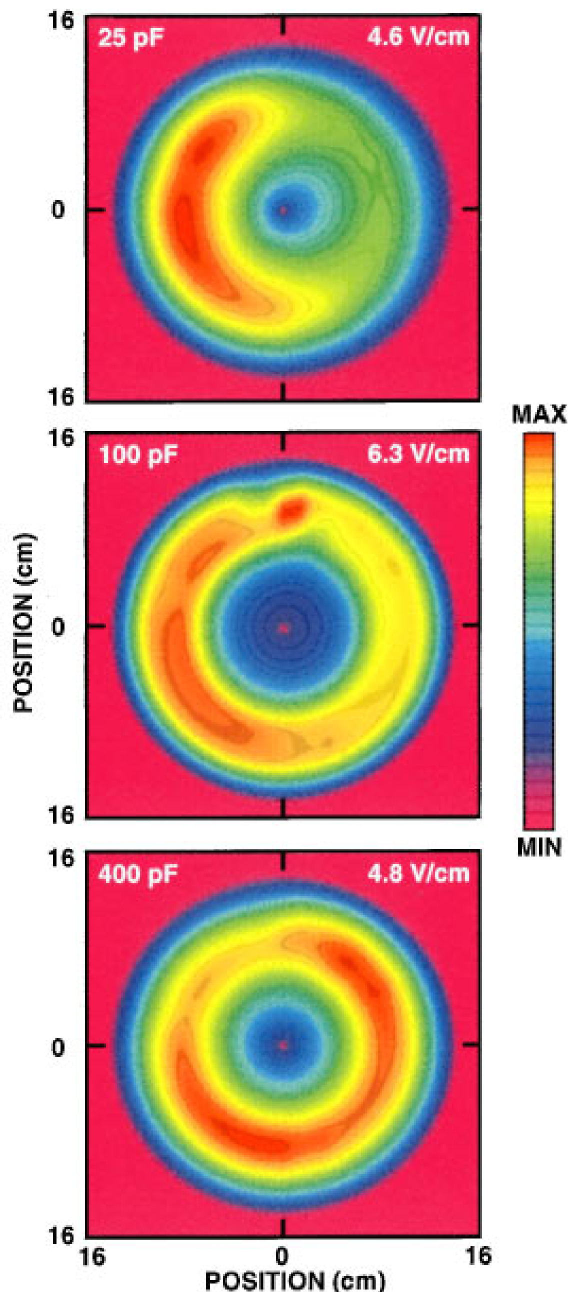

FIG. 2. Magnitude of the inductively coupled electric field in the plasma for a (r,θ) slice ≈0.5 cm below the quartz window. Results are shown for termination impedances of the coil of 25, 100, and 400 pF. The maximum value of the electric field is shown at the top. The azimuthal symmetry of the electric field improves with increasing termination capacitance while the peak in the electric field rotates in angle.

along the transmission line.[12] For example, the magnitude of the inductively coupled electric field in a plane ≈0.5 cm below the quartz window is shown in Fig. 2 for termination impedances of 25 pF, 100 pF, and 400 pF. The capacitive coupling of the coil is ≈1 pF/cm of length while the skin depth in the plasma is ≈1.5–2 cm. For these conditions, the symmetry of the electric field improves and the location of the maximum in the electric field rotates as the termination capacitance increases. Maximum electric fields range from 4.5 to 6.5 V/cm. Although, the electric fields are dominated by the azimuthal component, the radial, and axial components do make significant contributions. For example, the ''hot spot'' in the electric field at the top of the figure for the case using a 100 pF termination impedance corresponds to the radial coil segment joining the two annuli. The local minimum in electric field close to the ''hot spot'' corresponds to the gap in the coil in the outer turn. The scaling shown here, that of improved uniformity with increasing termination capacitance, is not a general result since the electric field parameters depend, for example, on the degree of capacitive coupling and geometry of the coils.

The scaling shown in Fig. 2 correlates well with the transmission line characteristics of the coil and plasma for a system in which the length of the coil is less than 1/4 wavelength. In the absence of the termination capacitance, the reactance of the coil is ≈390 Ω. With a small termination capacitance (25 pF), the termination reactance (≈480 Ω) is larger than that of the coil. The current should therefore decrease along the coil, producing a maximum in the electric field near the input, which is observed. For a large termination (400 pF), the termination reactance is smaller (≈30 Ω) than that of the coil. The current should therefore increase along the coil, producing an electric field which peaks nearer the termination, which is also observed.

The total ion density and electron temperature are shown in Fig. 3 for the Ar/N_2 plasma at different axial locations. [The heights of these (r,θ) ''slices'' are indicated by the double arrows in Figs. 1(e) and 1(f).] The outlines of structural members in the reactor are shown in white. The lowest (r,θ) slice is a few mm of above the wafer and within the confines of the wafer clamp. The highest (r,θ) slice is between the top of the load lock bay and the quartz window. The termination impedance is 80 pF and the capacitive coil coupling is ≈1 pF/cm. These circuit values and geometries were purposely chosen to demonstrate asymmetries in plasma conditions and should not be considered as being optimized in any way. These circuit values do, however, represent typical component values which are encountered in construction of the coils.

The electron temperature is 4.2–4.4 eV directly under the quartz window in an annular region corresponding to the annular electric field. There is, however, a peak in the electron temperature on the left side of the reactor under the quartz window where there is a peak in the electric field and power deposition (see Fig. 2). This electric field distribution produces a local maximum in both ion production and plasma potential. The high thermal conductivity of the plasma disperses the maximum in the electron temperature in the azimuthal direction and fills in the central cool region, so that near the substrate the electron temperature is significantly more uniform than near the quartz window. There remains, however, a vestige of the electron temperature ''hot spot'' as low as the plane of the wafer.

The ion density has a maximum value of $\approx 1.5\times 10^{11}$ cm^{-3} approximately 2.5 cm below the quartz window. Near the quartz window [the highest (r,θ) slice in Fig. 3], there is a local azimuthal maximum in the ion density in the lower left quadrant of the reactor, located near the azimuth where there is a peak in the electron temperature. The locally high electron temperature produces higher ionization rates at that

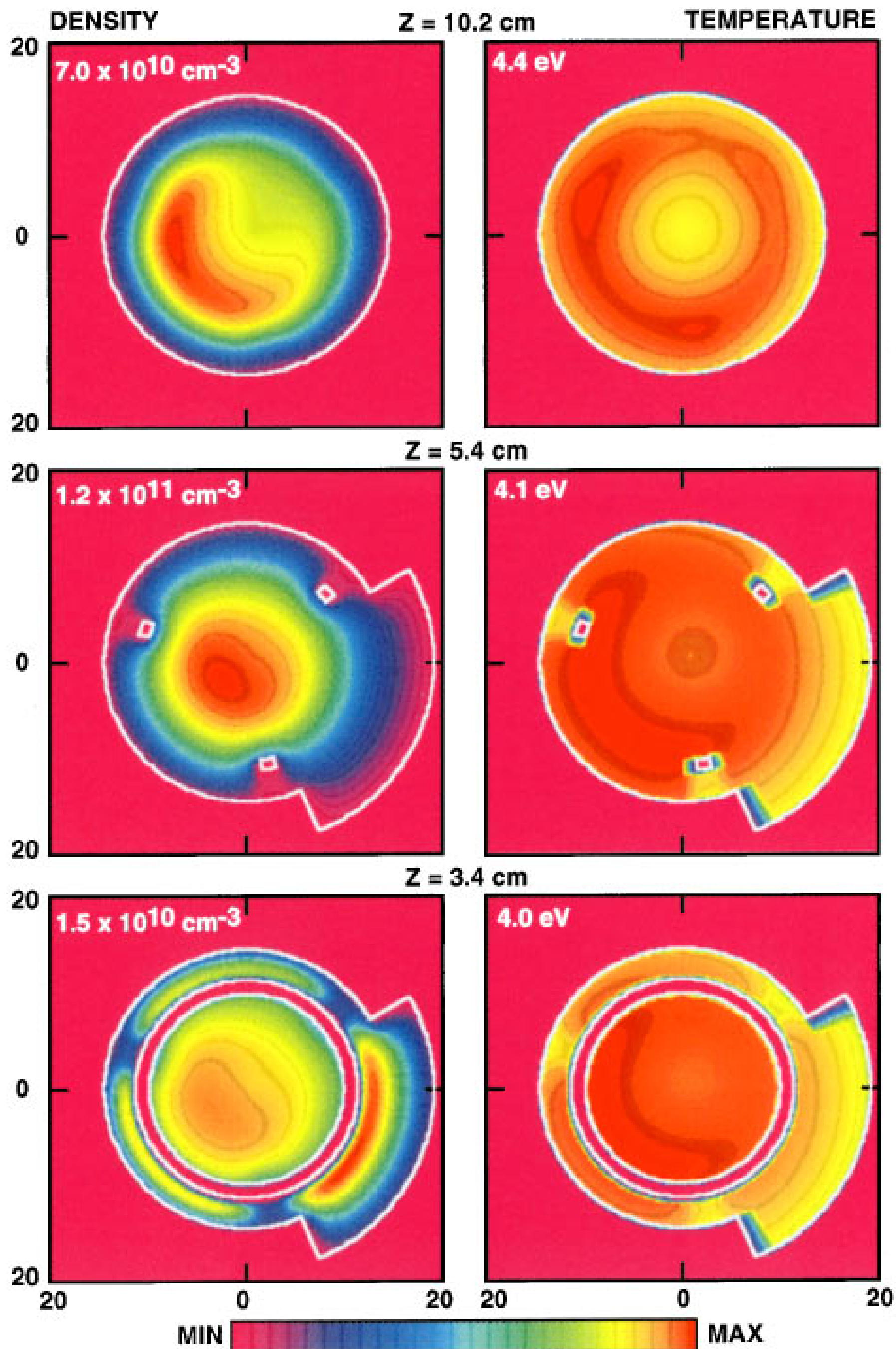

FIG. 3. Total ion density (left) and electron temperature (right) for (r,θ) slices at difference axial locations. The axial locations are shown by the double arrows in Figs. 1(e) and 1(f). The termination impedance 80 pF. The maximum value for the ion density or electron temperature in each frame is indicated in the figure. The local maximum in electric field just below the quartz window produces a maximum in power deposition, electron temperature, and ion source. The wafer clamp support structures and load lock opening perturb the plasma density by altering the local diffusion lengths.

location. The peak in the ionization rate near the quartz window, though dispersed by diffusion, is still evident at the plane of the wafer [the lowest (r,θ) slice in Fig. 3]. The wafer clamp support posts provide recombination surfaces for the plasma, which produce a lower plasma density extending a few cm beyond the posts. This can be seen in the middle (r,θ) slice in Fig. 3. The ion diffusion losses to the wafer clamp support structures contribute to lower ion densities at the plane wafer at their azimuths. The plasma density has a local maximum in the opening to the load lock bay. This local maximum is due to the locally longer diffusion length into the load lock bay which results in lower rates of ion loss to the walls. This also results in there being a lower rate of plasma loss from the volume above the wafer at those azimuthal locations. The end result is a small amount of ''skewing'' of the ion density towards the load lock bay opening.

The fact that the antenna generated azimuthal asymmetries in plasma production can persist to the plane of the wafer places added importance on proper coil design. To isolate these effects, experiments and modeling were per-

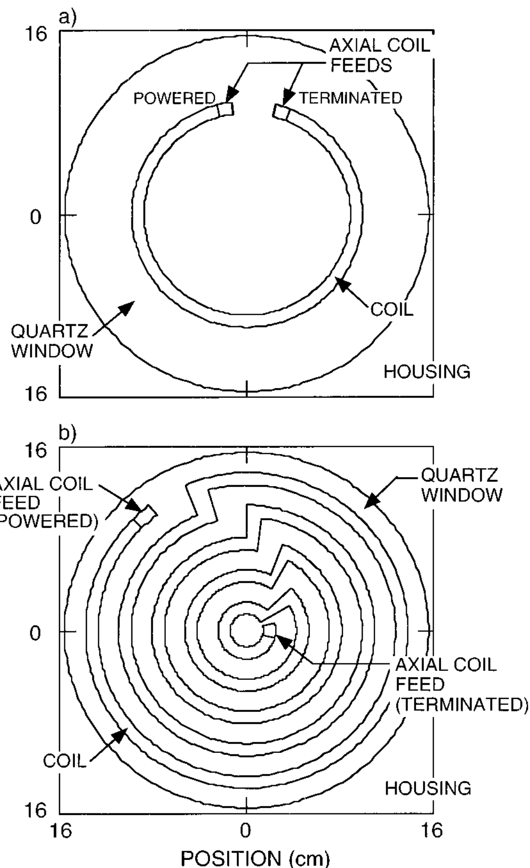

FIG. 4. Coil patterns for comparison of ICP reactors having (a) one-turn and (b) five-turn antennas. The location of the powered and terminated current feeds are shown. The coils are terminated with a 80 pF capacitor to ground.

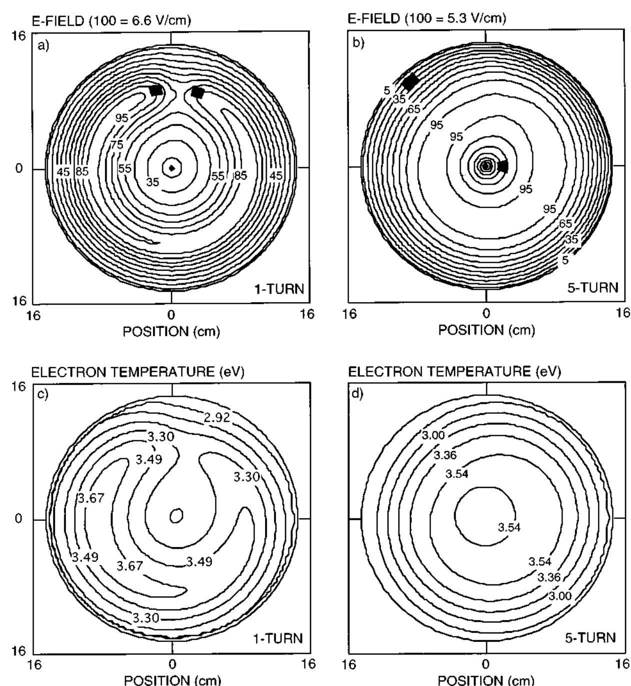

FIG. 5. Predicted parameters for ICP reactors having one-turn and five-turn coils. (a)–(b) Inductively coupled electric fields 0.5 cm below the quartz window and (c)–(d) electron temperature. The plasma conditions are 5 mTorr of Cl_2 and an ICP power deposition of 250 W. The contour labels are the percent of the maximum value indicated in each figure. For reference, the locations of the current feeds are indicated. The reactor having the one-turn coil produces an asymmetric electric field and a commensurate asymmetry in the electron temperature.

formed on an ICP reactor whose internal structures were symmetric in the azimuthal direction. For these cases, we removed the load lock bay and wafer clamp support structures from the computational geometry discussed above. The only asymmetries are with the coil. Two designs which use one- and five-turn coils were experimentally and computationally investigated. The plasmas were sustained in 5 mTorr of Cl_2 with 250 W of power deposition while etching 200 mm diam poly-silicon wafers. Ion densities were obtained by measuring ion saturation current with a Langmuir probe. In modeling these experiments, the species we included are Cl_2, Cl_2^+, Cl, Cl^+, Cl^-, and Cl*. The reaction mechanisms are the same as discussed in Ref. 7. The coil patterns we used in the simulation are shown in Fig. 4. The coils were terminated with 80 nF capacitors. The physical inductance of the one- and five-turn coils in the model were 1.0 μF and 3.6 μF with capacitive coupling of 1pF/cm, commensurate with experimental measurements of the electrical properties of the coils.

The computed inductively coupled electric fields and electron temperature for the one- and five-turn coils at a plane $\approx$0.5 cm under the quartz window are shown in Fig. 5. The electric field for the one-turn coil is asymmetric and has an amplitude 10%–15% higher on the side of the reactor adjacent to the powered current feed. The electric field for the five-turn coil is more uniform in the azimuth, but does have a small azimuthal maximum in the lower right quadrant. The azimuthal nonuniformities in electric field produce corresponding nonuniformities in the electron temperature. The electron temperature for the one-turn coil peaks on the left side of the reactor, while that for the five-turn coil is skewed towards the lower right quadrant.

These asymmetries in electron temperature produce asymmetries in ionization rate and ultimately ion densities which persist to the plane of the wafer. For example, experimental and model derived values for ion density as a function of azimuth are shown in Fig. 6 for the one- and five-turn coil reactors. These values are for ion densities $\approx$1 cm above the edge of the wafer. The azimuthal angle is measured with respect to the axial current feed on the powered side of the coil. For the one-turn coil, there is an azimuthal variation in ion density of approximately $\pm$20% whose maximum maps (in angle) to the maximum in electron temperature at the plane of the quartz window. The ion density with the five-turn coil is significantly more uniform as a function of azimuth.

For these plasma conditions, the poly-silicon etch rate is in the ''ion starved'' regime. Although, the etching is dominantly by neutral Cl atoms, the uniformity of etching is largely determined by the ion flux uniformity. This is particularly true in Cl_2 plasmas where the Cl atom has a low reactive sticking coefficient on side walls, and therefore has a fairly uniform distribution throughout the reactor even though it may be produced nonuniformly. Experimental

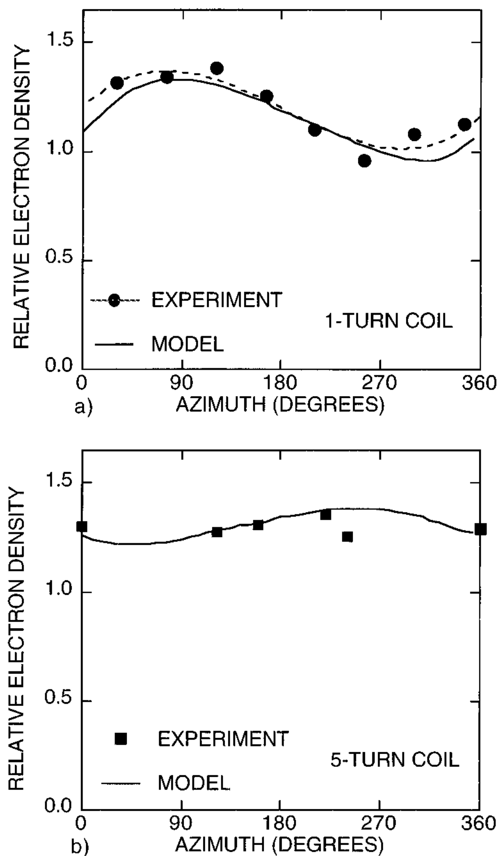

FIG. 6. Experiment and model derived ion densities 1 cm above the edge of the wafer as a function of azimuth location for (a) one-turn and (b) five-turn coils. The reactor with the one-turn coil has a significant azimuthal variation in the ion density. The discharge conditions are 5 mTorr of Cl_2 with 250 W ICP power.

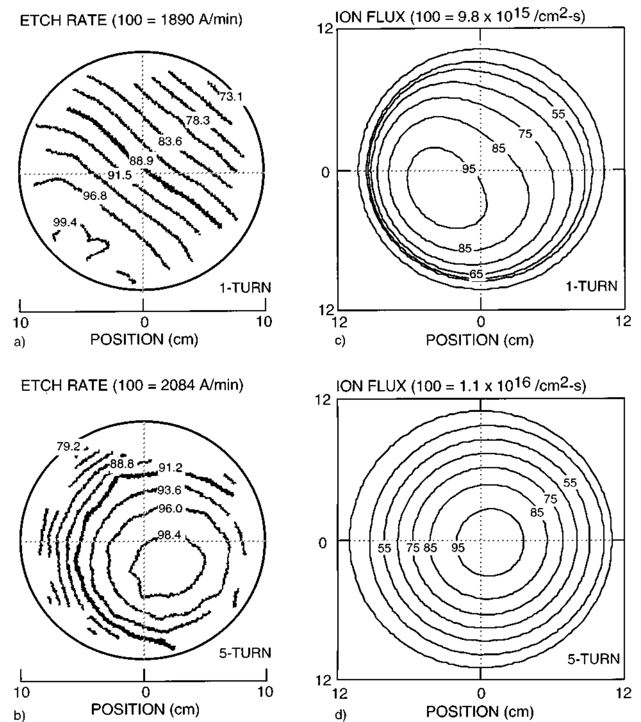

FIG. 7. Etch profiles and ion fluxes to the wafer for reactors having one- and five-turn coils with plasmas sustained in 5 mTorr of Cl_2 with 250 W ICP power. (a) and (b) Experimental etch rates for poly-silicon. (c) and (d) Predicted ion fluxes to the wafer.

measurements of the poly-silicon etch rates and model predictions for the ion flux to the wafer for the one- and five-turn coil geometries are shown in Fig. 7. The ion flux is the sum of the fluxes for Cl_2^+ and Cl^+. The peak etch rates are approximately 1890 Å/min for the one-turn coil and 2084 Å/min for the five-turn coil, a ratio of 1.1. The peak ion fluxes are 9.8×10^{15} and 1.1×10^{16} cm^{-2} s^{-1}, respectively, also a ratio of 1.1. For the one-turn coil, the etch rate shows a side-to-side variation, with the maximum at an azimuth corresponding to the peak in the calculated and measured ion density above the edge of the wafer. The ion flux to the wafer obtained from the model reproduces this trend. For the five-turn coil, the side-to-side variation in etch rate has been significantly reduced and the etch rate is more symmetric as a function of azimuth. There is, however, a shift in the center of symmetry of the etch rate to the right lower quadrant. The predicted ion flux to the wafer also has a shift towards the right lower quadrant. The azimuth at which the etch rate is a maximum maps to the azimuth of the maximum in the ion density. The small differences in the precise azimuth of the maxima in the experimental etch rates and predicted ion fluxes are due to small differences in the value of the termination impedence.

IV. CONCLUDING REMARKS

In conclusion, a three-dimensional model for inductively coupled plasma etching reactors has been presented. The consequences of coil design and asymmetries in the chamber construction on the plasma properties have been discussed. The uniformity of plasma production can be largely controlled by proper selection of circuit elements which determine the capacitive currents and standing wave pattern for the coil. We showed that azimuthal and side-to-side asymmetries in etch rates can be directly correlated to similar asymmetries in the inductively coupled electric field and ion production rates. These asymmetries persist to the plane of the wafer. Proper coil design can eliminate these asymmetries and produce azimuthally symmetric etching rates.

ACKNOWLEDGMENTS

The work performed at the University of Illinois was supported by Sandia National Laboratory/Sematech, the Semiconductor Research Corp., LAM Research Corp., the National Science Foundation (ECS 94-04133, CTS 94-12565), and the University of Wisconsin ERC for Plasma Aided Manufacturing.

[1] J. Hopwood, Plasma Sources Sci. Technol. **3**, 640 (1994).
[2] J. H. Keller, J. C. Forster, and M. S. Barnes, J. Vac. Sci. Technol. A **11**, 2487 (1993).
[3] M. S. Barnes, J. C. Forster, and J. H. Keller, Appl. Phys. Lett. **62**, 2622 (1993).
[4] R. Patrick, R. Schoenborn, and H. Toda, J. Vac. Sci. Technol. A **11**, 1296 (1993).

[5] L. J. Mahoney, A. E. Wendt, E. Barrios, C. J. Richards, and J. L. Shohet, J. Appl. Phys. **76**, 2041 (1994).
[6] J. Holland, V. Singh, F. Lin, and M. Barnes, Program of the 42nd Annual Symposium of the American Vacuum Society, Denver, CO, 1995 paper PS-TuP8 (unpublished), and J. Holland (private communication).
[7] P. L. G. Ventzek, M. J. Grapperhaus, and M. J. Kushner, J. Vac. Sci. Technol. B **12**, 3118 (1994).
[8] R. A. Stewart, P. Vitello, D. B. Graves, E. F. Jaeger, and L. A. Berry, Plasma Sources Sci. Technol. **4**, 36 (1995).
[9] G. Dipeso, V. Vahedi, D. W. Hewett, and T. D. Rognlien, J. Vac. Sci. Technol. A **12**, 1387 (1994).
[10] D. L. Lymberopoulos and D. Economou, Trans. Plasma Sci. **23**, 573 (1995).
[11] W. Collison and M. J. Kushner, Appl. Phys. Lett. **68**, 903 (1996).
[12] J. F. Jaeger, L. A. Berry, J. S. Tolliver, and D. B. Batchelor, J. Phys. Fluids **2**, 2597 (1995).
[13] R. B. Piejak, V. A. Godyak, and B. M. Alexandrovich, Plasma Sources Sci. Tech. **1**, 179 (1992).
[14] See, for example, W. L. Morgan and B. M. Penetrante, Comp. Phys. Comm. **58**, 127 (1990).
[15] T. J. Sommerer and M. J. Kushner, J. Appl. Phys. **71**, 1654 (1992).